RECAP: Towards Precise Radiology Report Generation via Dynamic Disease Progression Reasoning

Wenjun Hou[1,2], **Yi Cheng**[1*], **Kaishuai Xu**[1*], **Wenjie Li**[1†], **Jiang Liu**[2†]
[1]Department of Computing, The Hong Kong Polytechnic University, HKSAR, China
[2]Research Institute of Trustworthy Autonomous Systems and
Department of Computer Science and Engineering,
Southern University of Science and Technology, Shenzhen, China
houwenjun060@gmail.com
{alyssa.cheng, kaishuaii.xu}@connect.polyu.hk
cswjli@comp.polyu.edu.hk, liuj@sustech.edu.cn

Abstract

Automating radiology report generation can significantly alleviate radiologists' workloads. Previous research has primarily focused on realizing highly concise observations while neglecting the precise attributes that determine the severity of diseases (e.g., *small pleural effusion*). Since incorrect attributes will lead to imprecise radiology reports, strengthening the generation process with precise attribute modeling becomes necessary. Additionally, the temporal information contained in the historical records, which is crucial in evaluating a patient's current condition (e.g., *heart size is unchanged*), has also been largely disregarded. To address these issues, we propose RECAP, which generates precise and accurate radiology reports via dynamic disease progression reasoning. Specifically, RECAP first predicts the observations and progressions (i.e., spatiotemporal information) given two consecutive radiographs. It then combines the historical records, spatiotemporal information, and radiographs for report generation, where a disease progression graph and dynamic progression reasoning mechanism are devised to accurately select the attributes of each observation and progression. Extensive experiments on two publicly available datasets demonstrate the effectiveness of our model.[1]

1 Introduction

Radiology report generation (Rennie et al., 2017; Anderson et al., 2018; Chen et al., 2020), aiming to generate clinically coherent and factually accurate free-text reports, has received increasing attention from the research community due to its large potential to alleviate radiologists' workloads.

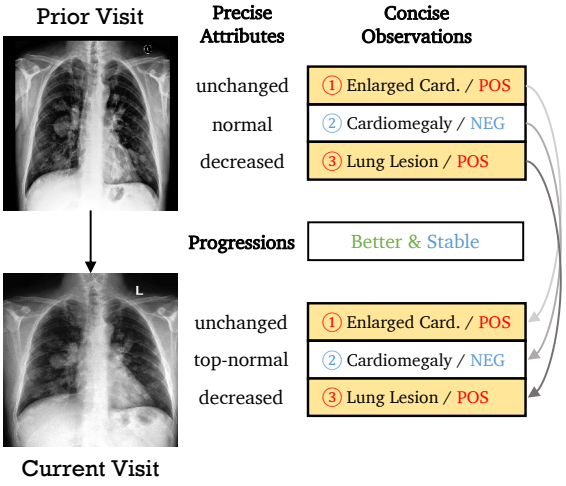

Figure 1: An example of a follow-up visit record with its prior visit record. Part of their observations are listed with their precise attributes. *Enlarged Card.* denotes *Enlarged Cardiomediastinum*.

Recent research works (Nooralahzadeh et al., 2021; Nishino et al., 2022; Delbrouck et al., 2022; Bannur et al., 2023; Tanida et al., 2023; Hou et al., 2023) have made significant efforts in improving the clinical factuality of generated reports. Despite their progress, these methods still struggle to produce precise and accurate free-text reports. One significant problem within these methods is that although they successfully captured the semantic information of observations, their attributes still remain imprecise. They either ignored historical records (i.e., temporal information) that are required for assessing patients' current conditions or omitted the fine-grained attributes of observations (i.e., spatial information) that are crucial in quantifying the severity of diseases, which are far from adequate and often lead to imprecise reports. Both

*Equal Contribution.
†Corresponding authors.
[1]Our code is available at https://github.com/wjhou/Recap.

Findings of the Association for Computational Linguistics: EMNLP 2023, pages 2134–2147
December 6-10, 2023

temporal and spatial information are crucial for generating precise and accurate reports. For instance, as illustrated in Figure 1, the patient's conditions can change from time to time, and the observations become `Better` and `Stable`. Only if accessing the historical records, the overall conditions could be estimated. In addition, different attributes reflect the severity of an observation, such as *normal* and *top-normal* for *Cardiomegaly*. In order to produce precise and accurate free-text reports, we must consider both kinds of information and apply stronger reasoning to strengthen the generation process with precise attribute modeling.

In this paper, we propose RECAP, which captures both temporal and spatial information for radiology REport Generation via DynamiC DiseAse Progression Reasoning. Specifically, RECAP first predicts observations and progressions given two consecutive radiographs. It then combines them with the historical records and the current radiograph for report generation. To achieve precise attribute modeling, we construct a disease progression graph, which contains the prior and current observations, the progressions, and the precise attributes. We then devise a dynamic progression reasoning (PrR) mechanism that aggregates information in the graph to select observation-relevant attributes.

In conclusion, our contributions can be summarized as follows:

- We propose RECAP, which can capture both spatial and temporal information for generating precise and accurate free-text reports.
- To achieve precise attribute modeling, we construct a disease progression graph containing both observations and fine-grained attributes that quantify the severity of diseases. Then, we devise a dynamic disease progression reasoning (PrR) mechanism to select observation/progression-relevant attributes.
- We conduct extensive experiments on two publicly available benchmarks, and experimental results demonstrate the effectiveness of our model in generating precise and accurate radiology reports.

2 Preliminary

2.1 Problem Formulation

Given a radiograph-report pair $D^c = \{X^c, Y^c\}$, with its record of last visit being either $D^p = \{X^p, Y^p\}$ or $D^p = \emptyset$ if the historical record is missing[2], the task of radiology report generation aims to maximize $p(Y^c|X^c, D^p)$. To learn the spatiotemporal information, observations O (i.e., spatial information) (Irvin et al., 2019) and progressions P (i.e., temporal information) (Wu et al., 2021) are introduced. Then, the report generation process is divided into two stages in our framework, i.e., observation and progression prediction (i.e., Stage 1) and spatiotemporal-aware report generation (i.e., Stage 2). Specifically, the probability of observations and progressions are denoted as $p(O|X^c)$ and $p(P|X^c, X^p)$, respectively, and then the generation process is modeled as $p(Y^c|X^c, D^p, O, P)$. Finally, our framework aims to maximize the following probability:

$$p(Y^c|X^c, D^p) \propto \overbrace{p(O|X^c) \cdot p(P|X^c, X^p)}^{\text{Stage 1}} \underbrace{\cdot p(Y^c|X^c, D^p, O, P)}_{\text{Stage 2}}.$$

2.2 Progression Graph Construction

Observation and Progression Extraction. For each report, we first label its observations $O = \{o_1, \ldots, o_{|O|}\}$ with CheXbert (Smit et al., 2020). Similar to Hou et al. (2023), each observation is further labeled with its status (i.e., *Positive*, *Negative*, *Uncertain*, and *Blank*). We convert *Positive* and *Uncertain* as POS, *Negative* as NEG, and remove *Blank*, as shown in Figure 1. Then, we extract progression information P of a patient with Chest ImaGenome (Wu et al., 2021) which provides progression labels (i.e., `Better`, `Stable`, or `Worse`) between two regions of interest (ROIs) in X^p and X^c, respectively. However, extracting ROIs could be difficult, and adopting such ROI-level labels may not generalize well across different datasets. Thus, we use image-level labels, which only indicate whether there are any progressions between X^p and X^c. As a result, a patient may have different progressions (e.g., both `Better` and `Worse`). The statistics of observations and progressions can be found in Appendix A.1.

Spatial/Temporal Entity (Attribute) Collection.[3] To model spatial and temporal information, we

[2]There are two kinds of records (i.e., first-visit and follow-up-visit). If it is the first visit of a patient, the historical record does not exist.

[3]Attributes are included in the entity set as provided by Jain et al. (2021). For simplicity, we use "attribute" and "entity" interchangeably in this paper.

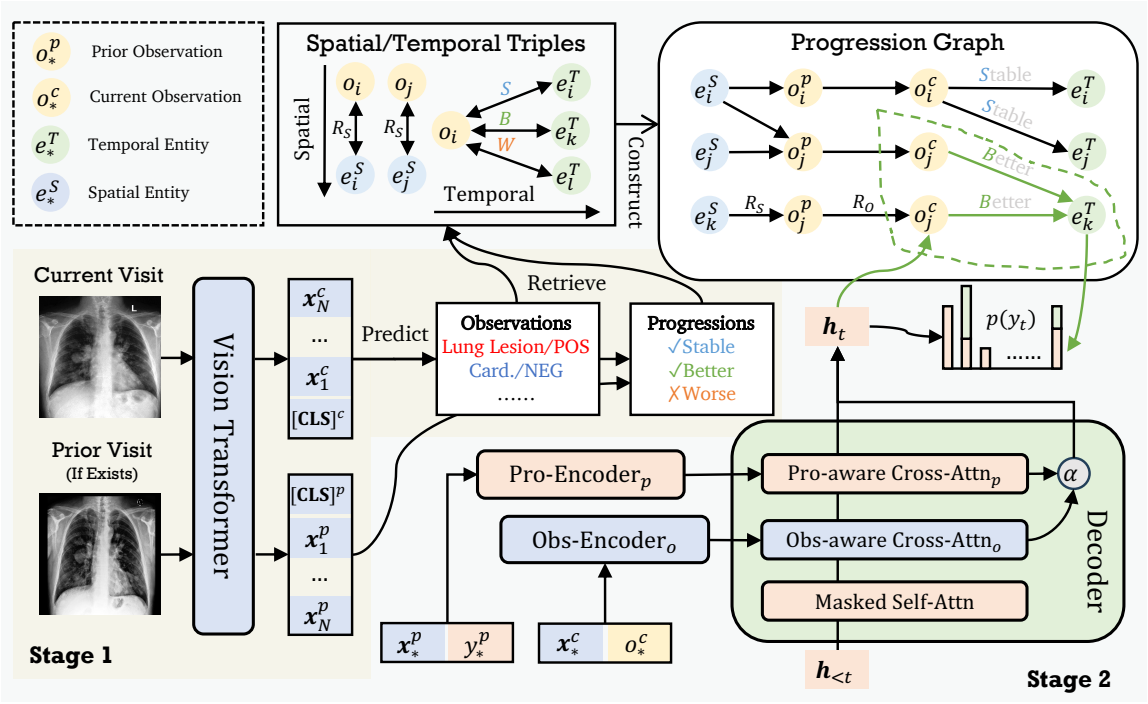

Figure 2: Overview of the RECAP framework. *Pro-Encoder*$_p$ is the progression-related encoder and *Obs-Encoder*$_o$ is the observation-related encoder, respectively. Other modules in the decoder are omitted for simplicity.

collect a set of entities to represent it. For temporal entities, we adopt the entities provided by (Bannur et al., 2023), denoted as E^T. For spatial entities E^S, we adopt the entities with a relation *modify* or *located_at* in RadGraph (Jain et al., 2021), and we also filter out stopwords[4] and temporal entities from them. Part of the temporal and spatial entities are listed in Appendix A.2.

Progression Graph Construction. Our progression graph $G =< V, R >$ is constructed based purely on the training corpus in an unsupervised manner. Specifically, $V = \{O, E^T, E^S\}$ is the node-set, and $R = \{S, B, W, R_S, R_O\}$ is the edge set, where S, B, and W denote three progressions `Stable`, `Better`, and `Worse`, connecting an observation with an temporal entity. In addition, R_s and R_o are additional relations connecting current observations with spatial entities and prior/current observations, respectively. To extract spatial/temporal triples automatically, we use the proven-efficient statistical tool, i.e., pointwise mutual information (PMI; Church and Hanks (1990)), where a higher PMI score implies two units with higher co-occurrence, similar to Hou et al. (2023):

$$\text{PMI}(\bar{x}, \hat{x}) = \log \frac{p(\bar{x}, \hat{x})}{p(\bar{x})p(\hat{x})} = \log \frac{p(\hat{x}|\bar{x})}{p(\hat{x})},$$

Specifically, we set $\bar{x}$ to (o_i, r_j) where $r_j \in R$ and set $\hat{x}$ to e_k^* where $e_k^* \in \{E^T, E^S\}$. Then, we rank these triples using PMI$((o_i, r_j), e_k^*)$ and select top-K of them as candidates for each (o_i, r_j). Finally, we use observations as the query to retrieve relevant triples. We consider edges in the graph: $e_i^* \xrightarrow{r_j} o_k^p \xrightarrow{R_O} o_l^c \xrightarrow{r_m} e_n^*$, as shown in the top-right of Figure 2, consistent with the progression direction.

[4] https://www.nltk.org/

3 Methodology

3.1 Visual Encoding

Given an image X^c, an image processor is first to split it into N patches, and then a visual encoder (i.e., ViT (Dosovitskiy et al., 2021)) is adopted to extract visual representations $\boldsymbol{X}^c$:

$$\boldsymbol{X}^c = \{[\textbf{CLS}]^c, \boldsymbol{x}_1^c, \ldots, \boldsymbol{x}_N^c\} = \text{ViT}(X^c),$$

where $[\textbf{CLS}]^c \in \mathbb{R}^h$ is the representation of the class token `[CLS]` prepended in the patch sequence, $\boldsymbol{x}_i^c \in \mathbb{R}^h$ is the i-th visual representation. Similarly, the visual representation of image X^p is extracted using the same ViT model and represented as $\boldsymbol{X}^p = \{[\textbf{CLS}]^p, \boldsymbol{x}_1^p, \ldots, \boldsymbol{x}_N^p\}$.

3.2 Stage 1: Observation and Progression Prediction

Observation Prediction. As observations can be measured from a single image solely, we only use the pooler output $[\textbf{CLS}]^c$ of X^c for observation

prediction. Inspired by Tanida et al. (2023), we divide it into two steps, i.e., detection and then classification. Specifically, the detection probability $p_d(o_i)$ of the i-th observation presented in a report and the probability of this observation $p_c(o_i)$ being classified as abnormal are modeled as:

$$p_d(o_i) = \sigma(\boldsymbol{W}_{d_i}[\textbf{CLS}]^c + b_{d_i}),$$
$$p_c(o_i) = \sigma(\boldsymbol{W}_{c_i}[\textbf{CLS}]^c + b_{c_i}),$$

where σ is the Sigmoid function, $\boldsymbol{W}_{d_i}$,$\boldsymbol{W}_{c_i} \in \mathbb{R}^h$ are the weight matrices and $b_{d_i}, b_{c_i} \in \mathbb{R}$ are the biases. Finally, the probability of the i-th observation is denoted as $p(o_i) = p_d(o_i) \cdot p_c(o_i)$. Note that for observation *No Finding* o_n is presented in every sample, i.e., $p_d(o_n) = 1$ and $p(o_n) = p_c(o_n)$.

Progression Prediction. Similar to observation prediction, the pooler outputs $[\textbf{CLS}]^p$ of X^p and $[\textbf{CLS}]^c$ of X^c are adopted for progression prediction, and the probability of the j-th progression $p(p_j)$ is modeled as:

$$[\textbf{CLS}] = [[\textbf{CLS}]^p; [\textbf{CLS}]^c],$$
$$p(p_j) = \sigma(\boldsymbol{W}_j[\textbf{CLS}] + b_j),$$

where $[;]$ is the concatenation operation, $\boldsymbol{W}_j \in \mathbb{R}^{2h}$ is the weight matrix, and $b_j \in \mathbb{R}$ are the bias. As we found that learning sparse signals from image-level progression labels is difficult and has side effects on the performance of observation prediction, we detach [**CLS**] from the computational graph while training.

Training. We optimize these two prediction tasks by minimizing the binary cross-entropy loss. Specifically, the loss of observation detection $\mathcal{L}_d$ is denoted as:

$$\mathcal{L}_d = -\frac{1}{|O|}\sum[\alpha_d \cdot l_{d_i} \cdot \log p_d(o_i) + (1 - l_{d_i}) \cdot \log(1 - p_d(o_i))],$$

where α_d is the weight to tackle the class imbalance issue, l_{d_i} denotes the label of i-th observation d_i. Similarly, the loss of observation classification $\mathcal{L}_c$ and progression prediction $\mathcal{L}_p$ can be calculated using the above equation. Note that $\mathcal{L}_c$ and $\mathcal{L}_p$ are unweighted loss. Finally, the overall loss of Stage 1 is $\mathcal{L}_{S1} = \mathcal{L}_d + \mathcal{L}_c + \mathcal{L}_p$.

3.3 Stage 2: SpatioTemporal-aware Report Generation

Observation-aware Visual Encoding. To learn the observation-aware visual representations, we jointly encode $\boldsymbol{X}^c$ and its observations O^c using a Transformer encoder (Vaswani et al., 2017). Additionally, a special token `[FiV]` for first-visit records or `[FoV]` for follow-up-visit records is appended to distinguish them, represented as `[F*V]`:

$$\boldsymbol{h}^c = [\boldsymbol{h}^c_X; \boldsymbol{h}^c_o] = \text{Encoder}_o([\boldsymbol{X}^c; \texttt{[F*V]}; O^c]),$$

where $\boldsymbol{h}^c_X, \boldsymbol{h}^c_o \in \mathbb{R}^h$ are the visual hidden representations and observation hidden representations of the current radiograph and observations.

Progression-aware Information Encoding. We use another encoder to encode the progression information (i.e., temporal information). Specifically, given $\boldsymbol{X}^p$ and Y^p, the hidden states of the prior record are represented as:

$$\boldsymbol{h}^p = [\boldsymbol{h}^p_X; \boldsymbol{h}^p_Y] = \text{Encoder}_p([\boldsymbol{X}^p; Y^p]),$$

where $\boldsymbol{h}^p_X, \boldsymbol{h}^p_Y \in \mathbb{R}^h$ are the visual hidden representations and textual hidden representations of prior records, respectively.

Concise Report Decoding. Given $\boldsymbol{h}^p$ and $\boldsymbol{h}^c$, a Transformer decoder is adopted for report generation. Since not every sample has a prior record and follow-up records may include new observations, controlling the progression information is necessary. Thus, we include a soft gate α to fuse the observation-related and progression-related information, as shown in Figure 2:

$$\text{Decoder} = \begin{cases} \boldsymbol{h}^s_t = \text{Self-Attn}(\boldsymbol{h}^w_t, \boldsymbol{h}^w_{<t}, \boldsymbol{h}^w_{<t}), \\ \tilde{\boldsymbol{h}}^c_t = \text{Cross-Attn}_o(\boldsymbol{h}^s_t, \boldsymbol{h}^c, \boldsymbol{h}^c), \\ \tilde{\boldsymbol{h}}^p_t = \text{Cross-Attn}_p(\tilde{\boldsymbol{h}}^c_t, \boldsymbol{h}^p, \boldsymbol{h}^p), \\ \alpha = \sigma(\boldsymbol{W}_\alpha \tilde{\boldsymbol{h}}^c_t + b_\alpha), \\ \boldsymbol{h}_t = \alpha \cdot \tilde{\boldsymbol{h}}^p_t + (1 - \alpha) \cdot \tilde{\boldsymbol{h}}^c_t, \end{cases}$$
$$p_\mathcal{V}(y_t) = \text{Softmax}(\boldsymbol{W}_\mathcal{V}\boldsymbol{h}_t + \boldsymbol{b}_\mathcal{V}),$$

where Self-Attn is the self-attention module, Cross-Attn is the cross-attention module, $\boldsymbol{h}^s_t, \tilde{\boldsymbol{h}}^c_t, \tilde{\boldsymbol{h}}^p_t, \boldsymbol{h}_t \in \mathbb{R}^h$ are self-attended hidden state, observation-related hidden state, progression-related hidden state, and spatiotemporal-aware hidden state, respectively, $\boldsymbol{W}_\alpha \in \mathbb{R}^h, \boldsymbol{W}_\mathcal{V} \in \mathbb{R}^{|\mathcal{V}| \times h}$ are weight matrices and $b_\alpha \in \mathbb{R}, \boldsymbol{b}_\mathcal{V} \in \mathbb{R}^{|\mathcal{V}|}$ are the biases.

Disease Progression Encoding. As there are different relations between nodes, we adopt an L-layer Relational Graph Convolutional Network (R-GCN) (Schlichtkrull et al., 2018) to encode the disease progression graph, similar to Ji et al. (2020):

$$\boldsymbol{h}^{l+1}_{v_i} = \text{ReLU}\left(\frac{1}{c_i}\sum_{v_k \in V}^{r_j \in R} \boldsymbol{W}^l_{r_j}\boldsymbol{h}^l_{v_k} + \boldsymbol{W}^l_0\boldsymbol{h}^l_{v_i}\right),$$

where c_i is the number of neighbors connected to the i-th node, $\boldsymbol{W}^l_{r_j}, \boldsymbol{W}^l_0 \in \mathbb{R}^{h \times h}$ are learnable weight metrics, and $\boldsymbol{h}^l_{v_i}, \boldsymbol{h}^{l+1}_{v_i}, \boldsymbol{h}^l_{v_k} \in \mathbb{R}^h$ are the hidden representations.

Dataset	Model	NLG Metrics						CE Metrics		
		B-1	B-2	B-3	B-4	MTR	R-L	P	R	F_1
MIMIC -ABN	R2GEN	0.290	0.157	0.093	0.061	0.105	0.208	0.266	0.320	0.272
	R2GENCMN	0.264	0.140	0.085	0.056	0.098	0.212	0.290	0.319	0.280
	ORGAN	0.314	0.180	0.114	0.078	**0.120**	**0.234**	0.271	0.342	0.293
	RECAP (Ours)	**0.321**	**0.182**	**0.116**	**0.080**	**0.120**	0.223	**0.300**	**0.363**	**0.305**
MIMIC -CXR	R2GEN	0.353	0.218	0.145	0.103	0.142	0.270	0.333	0.273	0.276
	R2GENCMN	0.353	0.218	0.148	0.106	0.142	0.278	0.344	0.275	0.278
	$\mathcal{M}^2$TR	0.378	0.232	0.154	0.107	0.145	0.272	0.240	0.428	0.308
	KNOWMAT	0.363	0.228	0.156	0.115	–	0.284	**0.458**	0.348	0.371
	CMM-RL	0.381	0.232	0.155	0.109	0.151	0.287	0.342	0.294	0.292
	CMCA	0.360	0.227	0.156	0.117	0.148	0.287	0.444	0.297	0.356
	KiUT	0.393	0.243	0.159	0.113	0.160	0.285	0.371	0.318	0.321
	DCL	–	–	–	0.109	0.150	0.284	0.471	0.352	0.373
	METrans	0.386	0.250	0.169	0.124	0.152	0.291	0.364	0.309	0.311
	ORGAN	0.407	0.256	0.172	0.123	0.162	**0.293**	0.416	0.418	0.385
	RECAP (Ours)	**0.429**	**0.267**	**0.177**	**0.125**	**0.168**	0.288	0.389	**0.443**	**0.393**

Table 1: Experimental Results of our model and baselines on the MIMIC-ABN and MIMIC-CXR datasets. The best results are in **boldface**, and the underlined are the second-best results. The experimental results on the MIMIC-ABN dataset are replicated based on their corresponding repositories.

Precise Report Decoding via Progression Reasoning. Inspired by Ji et al. (2020) and Mu and Li (2022), we devise a dynamic disease progression reasoning (PrR) mechanism to select observation-relevant attributes from the progression graph. The reasoning path of PrR is $o_i^c \xrightarrow{r_j} e_k$, where r_j belongs to either three kinds of progression or R_s. Specifically, given t-th hidden representation $\boldsymbol{h}_t$, the observation representation $\boldsymbol{h}_{o_i}^L$, and the entity representation $\boldsymbol{h}_{e_k}^L$ of e_k, the progression score $\hat{ps}_t(e_k)$ of node e_k is calculated as:

$$ps_t(e_k) = \frac{1}{|\mathcal{N}_{e_k}|} \sum_{(o_i, r_j) \in \mathcal{N}_{e_k}} \phi(\boldsymbol{h}_t^\top \boldsymbol{W}_{r_i} [\boldsymbol{h}_{o_i}^L ; \boldsymbol{h}_{e_k}^L]),$$

$$\hat{ps}_t(e_k) = \gamma \cdot ps_t(e_k) + \phi(\boldsymbol{h}_t \boldsymbol{W}_s \boldsymbol{h}_{e_k}^L),$$

where ϕ is the Tangent function, γ is the scale factor, $\mathcal{N}_{e_k}$ is the neighbor collection of e_k, and $\boldsymbol{W}_{r_i} \in \mathbb{R}^{h \times 2h}$ and $\boldsymbol{W}_s \in \mathbb{R}^{h \times h}$ are weight matrices for learning relation r_i and self-connection, respectively. In the PrR mechanism, the relevant scores (i.e., $ps_t(e_k)$) of their connected observations are also included in $\hat{ps}_t(e_k)$ since $\boldsymbol{h}_t$ contains observation information, and higher relevant scores of these connected observations indicate a higher relevant score of e_k. Then, the distribution over all entities in G is denoted as:

$$p_G(y_t) = \text{Softmax}(\hat{ps}_t(e_k)).$$

Finally, a soft gate $g_t = \sigma(\boldsymbol{W}_g \boldsymbol{h}_t + b_g)$ is adopted to combine $p_{\mathcal{V}}(y_t)$ and $p_G(y_t)$ into $p(y_t)$:

$$p(y_t) = g_t \cdot p_{\mathcal{V}}(y_t) + (1 - g_t) \cdot p_G(y_t),$$

where $\boldsymbol{W}_g \in \mathbb{R}^h$ and $b_g \in \mathbb{R}$ are the weight matrix and bias, respectively.

Training. The generation process is optimized using the negative log-likelihood loss, given each token's probability $p(y_t)$ and the probability of g_t:

$$\mathcal{L}_{\text{NLL}} = -\sum_{t=1}^{T} \log p(y_t),$$

$$\mathcal{L}_g = -\sum_{t=1}^{T} [l_{g_t} \log g_t + (1 - l_{g_t}) \log(1 - g_t)],$$

where l_{g_t} indicates t-th token appears in G. Finally, the loss of Stage 2 is $\mathcal{L}_{S2} = \mathcal{L}_{\text{NLL}} + \lambda \mathcal{L}_g$.

4 Experiments

4.1 Datasets

We use two benchmarks to evaluate our models, MIMIC-ABN[5] (Ni et al., 2020) and MIMIC-CXR[6] (Johnson et al., 2019). We provide other details of data preprocessing in Appendix A.3.

- MIMIC-CXR consists of 377,110 chest X-ray images and 227,827 reports from 63,478 patients. We adopt the settings of Chen et al. (2020).

[5] https://github.com/zzxslp/WCL

[6] https://physionet.org/content/mimic-cxr-jpg/2.0.0/

Model	Sections	B-2	CE-F_1
R2GEN	*Find. & Imp.*	0.212	0.148
IFCC	*Findings*	0.217	0.270
CXR-RePaiR-Sel	*Impressions*	0.050	0.274
BioViL-T	*Impressions*	0.159	0.348
BioViL-T	*Find. & Imp.*	0.213	0.359
ORGAN	*Findings*	0.267	0.385
RECAP (Ours)	*Findings*	**0.265**	**0.393**

Table 2: BLEU score and CheXbert score of our model and baselines on the MIMIC-CXR dataset. Results are cited from Bannur et al. (2023) and Hou et al. (2023).

- MIMIC-ABN is a modified version of MIMIC-CXR and only contains abnormal sentences. The original train/validation/test split of Ni et al. (2020) is 26,946/3,801/7,804 samples, respectively. To collect patients' historical information and avoid information leakage, we recover the data-split used in MIMIC-CXR according to the *subject_id*[7]. Finally, the data-split used in our experiments is 71,786/546/806 for train/validation/test sets, respectively.

4.2 Evaluation Metrics and Baselines

NLG Metrics. BLEU (Papineni et al., 2002), METEOR (Banerjee and Lavie, 2005), and ROUGE (Lin, 2004) are selected as the Natural Language Generation metrics (NLG Metrics), and we use the MS-COCO evaluation tool[8] to compute the results.
CE Metrics. For Clinical Efficacy (CE Metrics), CheXbert[9] (Smit et al., 2020) is adopted to label the generated reports compared with disease labels of the references. Besides, we use the temporal entity matching scores (TEM), proposed by Bannur et al. (2023), to evaluate how well the models generate progression-related information.
Baselines. For performance evaluation, we compare our model with the following state-of-the-art (SOTA) baselines: R2GEN (Chen et al., 2020), R2GENCMN (Chen et al., 2021), KNOWMAT (Yang et al., 2021), $\mathcal{M}^2$TR (Nooralahzadeh et al., 2021), CMM-RL (Qin and Song, 2022), CMCA (Song et al., 2022), CXR-RePaiR-Sel/2 (Endo et al., 2021), BioViL-T (Bannur et al., 2023), DCL (Li et al., 2023), METrans (Wang et al., 2023), KiUT (Huang et al., 2023), and ORGAN (Hou et al., 2023).

[7] *subject_id* is the anonymized identifier of a patient.
[8] https://github.com/tylin/coco-caption
[9] https://github.com/stanfordmlgroup/CheXbert

Model	B-4	R-L	CE-F_1	TEM
CXR-RePaiR-2	0.021	0.143	0.281	0.125
BioViL-NN	0.037	0.200	0.283	0.111
BioViL-T-NN	0.045	0.205	0.290	0.130
BioViL-AR	0.075	0.279	0.293	0.138
BioViL-T-AR	0.092	**0.296**	0.317	0.175
RECAP (Ours)	**0.118**	0.279	0.400	**0.304**
RECAP *w/o* OP	0.093	0.260	0.256	0.203
RECAP *w/o* Obs	0.104	0.270	0.307	0.240
RECAP *w/o* Pro	0.103	0.266	0.395	0.269
RECAP *w/o* PrR	0.115	0.279	**0.403**	0.296

Table 3: Progression modeling performance of our model and baselines on the MIMIC-CXR dataset. The *-NN models use nearest neighbor search for report generation, and the *-AR models use autoregressive decoding, as indicated in Bannur et al. (2023).

4.3 Implementation Details

We use the ViT (Dosovitskiy et al., 2021), a vision transformer pretrained on ImageNet (Deng et al., 2009), as the visual encoder[10]. The maximum decoding step is set to 64/104 for MIMIC-ABN and MIMIC-CXR, respectively. γ is set to 2 and K is set to 30 for both datasets.

For model training, we adopt AdamW (Loshchilov and Hutter, 2019) as the optimizer. The layer number of the Transformer encoder and decoder are both set to 3, and the dimension of the hidden state is set to 768, which is the same as the one of ViT. The layer number L of the R-GCN is set to 3. The learning rate is set to 5e-5 and 1e-4 for the pretrained ViT and the rest of the parameters, respectively. The learning rate decreases from the initial learning rate to 0 with a linear scheduler. The dropout rate is set to 0.1, the batch size is set to 32, and λ is set to 0.5. We select the best checkpoints based on the BLEU-4 on the validation set. Our model has 160.05M trainable parameters, and the implementations are based on the HuggingFace's *Transformers* (Wolf et al., 2020). We implement our models on an NVIDIA-3090 GTX GPU with mixed precision. Other details of implementation (e.g., Stage 1 training) can be found in Appendix A.3.

5 Results

5.1 Quantitative Analysis

NLG Results. The NLG results of two datasets are listed on the left side of Table 1 and Table 2. As we can see from Table 1, RECAP achieves the best

[10] The model card is "google/vit-base-patch16-224-in21k."

Dataset	Model	NLG Metrics						CE Metrics		
		B-1	B-2	B-3	B-4	MTR	R-L	P	R	F_1
MIMIC-ABN	RECAP	0.321	0.182	0.116	0.080	0.120	0.223	0.300	0.363	0.305
	RECAP *w/o* OP	0.303	0.170	0.109	0.074	0.113	0.227	0.289	0.300	0.280
	RECAP *w/o* Obs	0.302	0.174	0.114	0.079	0.114	0.231	0.341	0.314	0.282
	RECAP *w/o* Pro	0.306	0.169	0.107	0.072	0.114	0.220	0.298	0.361	0.298
	RECAP *w/o* PrR	0.320	0.180	0.115	0.079	0.120	0.224	0.295	0.365	0.301
MIMIC-CXR	RECAP	0.429	0.267	0.177	0.125	0.168	0.288	0.389	0.443	0.393
	RECAP *w/o* OP	0.350	0.219	0.150	0.109	0.140	0.278	0.356	0.259	0.266
	RECAP *w/o* Obs	0.356	0.224	0.153	0.113	0.144	0.283	0.464	0.281	0.296
	RECAP *w/o* Pro	0.402	0.245	0.161	0.112	0.157	0.278	0.379	0.433	0.386
	RECAP *w/o* PrR	0.415	0.257	0.171	0.119	0.164	0.285	0.381	0.443	0.391

Table 4: Ablation results of our model and its variants. RECAP *w/o* OP is the standard Transformer model, *w/o* Obs stands for without observation, and *w/o* Pro stands for without progression.

performance compared with other SOTA models and outperforms other baselines substantially on both datasets.

Clinical Efficacy Results. The clinical efficacy results are shown on the right side of Table 1. RECAP achieves SOTA performance on F_1 score, leading to a 1.2% improvement over the best baseline (i.e., ORGAN) on the MIMIC-ABN dataset. Similarly, on the MIMIC-CXR dataset, our model achieves a score of 0.393, increasing by 0.8% compared with the second-best. This demonstrates that RECAP can generate better clinically accurate reports.

Temporal-related Results. Since there are only 10% follow-up-visits records in the MIMIC-ABN dataset, we mainly focus on analyzing the MIMIC-CXR dataset, as shown in Table 3 and Table 6. RECAP achieves the best performance on BLEU-4, TEM. In terms of the clinical F_1, RECAP *w/o* PrR outperforms other baselines. This indicates that historical records are necessary for generating follow-up reports.

Ablation Results. We perform ablation analysis, and the ablation results are listed in Table 4. We also list the ablation results on progression modeling in Table 6. There are four variants: (1) RECAP *w/o* OP (i.e., a standard Transformer model, removing spatiotemporal information), (2) RECAP *w/o* Obs (i.e., without observation), (3) RECAP *w/o* Pro (i.e., without progression), and (4) RECAP *w/o* PrR, which does not adopt the disease progression reasoning mechanism.

As we can see from Table 4, without the spatiotemporal information (i.e., variant 1), the performances drop significantly on both datasets, which indicates the necessity of spatiotemporal modeling in free-text report generation. In addition, compared with variant 1, the performance of RECAP *w/o* Obs increases substantially on the MIMIC-CXR dataset, which demonstrates the importance of historical records in assessing the current conditions of patients. In terms of CE metrics, learning from the observation information boosts the performance of RECAP drastically, with an improvement of 12%. In addition, the performance of RECAP increases compared with variant *w/o* PrR. This indicates that PrR can help generate precise and accurate reports.

5.2 Qualitative Analysis

Case Study. We conduct a detailed case study on how RECAP generates precise and accurate attributes of a given radiograph in Figure 3. RECAP successfully generates six observations, including five abnormal observations. Regarding attribute modeling, our model can generate the precise description "*the lungs are clear without focal consolidation*", which also appears in the reference, while RECAP *w/o* OP can not generate relevant descriptions. This indicates that spatiotemporal information plays a vital role in the generation process. Additionally, RECAP can learn to compare with the historical records (e.g., *mediastinal contours are stable and remarkable*) so as to precisely measure the observations.

Error Analysis. We depict error analysis to provide more insights, as shown in Figure 4. There are two major errors, which are false-positive observations (i.e., Positive Lung Opacity and Positive Pleural Effusion) and false-negative observations (i.e., Negative Cardiomegaly). Improving the performance of observation prediction could be an important direction in enhancing the quality of gener-

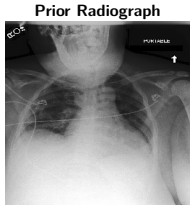

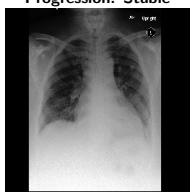

① Enlarged Card./NEG
② Cardiomegaly/POS
③ Edema/NEG
④ Consolidation/NEG
⑤ Pneumothorax/NEG
⑥ Pleural Effusion/NEG

Prior Report: low lung volumes are present. ② this accentuates the size of the cardiac silhouette which is likely mildly enlarged. ① mediastinal and hilar contours are likely within normal limits. a right brachiocephalic venous stent is re-demonstrated. there is crowding of the bronchovascular structures with probable ③ mild pulmonary vascular congestion. ⑥ no pleural effusion or ⑤ pneumothorax is identified.

Reference: ap and lateral views of the chest. the lungs are ④ **clear** of consolidation or ⑥ effusion. ② the cardiac silhouette is **enlarged** but **unchanged**. no acute osseous abnormality is detected. right brachiocephalic venous stent is again noted.

Ours: the lungs are **clear** without focal consolidation. no pleural effusion or pneumothorax is seen. the cardiac silhouette is **top-normal** to **mildly enlarged**. mediastinal contours are **stable** and **unremarkable**. there is no pulmonary edema.

Ours *w/o* OP: ap upright and lateral views of the chest provided. lung volumes are **low** limiting assessment. allowing for this there is ④ no focal consolidation ⑥ effusion or ⑤ pneumothorax. ① the cardiomediastinal silhouette is **normal**. imaged osseous structures are **intact**. no free air below the right hemidiaphragm is seen.

Figure 3: Case study of a follow-up-visit sample, given its prior radiograph and prior report. Attributes of observations in reports are highlighted in **boldface**, and spans with colors in reports indicate mentions of observations.

① Enlarged Card./NEG
② Cardiomegaly/F.NEG
③ Lung Opacity/F.POS
④ Pneumothorax/NEG
⑤ Effusion/F.POS

Reference: there is no new consolidation. right lower lobe pneumonia that was present in prior exams has significantly improved. esophageal stent is in unchanged position. there is no pneumomediastinum or pneumothorax. there is no pleural effusion . mediastinal and cardiac contours are stable.

Ours: ② the heart size is normal. the hilar and mediastinal contours are within normal limits. there is no pneumothorax. again seen is a ⑤ small right pleural effusion. the visualized osseous structures are unremarkable. there has been interval improvement of the ③ right basilar opacity.

Figure 4: Error case generated by RECAP. The span and the spans denote false negative observation and false positive observation, respectively.

ated reports. In addition, although RECAP aims to model precise attributes of observations presented in the radiograph, it still can not cover all the cases. This might be alleviated by incorporating external knowledge.

6 Related Work

6.1 Medical Report Generation

Medical report generation(Jing et al., 2018; Li et al., 2018), as one kind of image captioning (Vinyals et al., 2015; Rennie et al., 2017; Lu et al., 2017; Anderson et al., 2018), has received increasing attention from the research community. Some works focus on recording key information of the generation process via memory mechanism (Chen et al., 2020, 2021; Qin and Song, 2022; Wang et al., 2023). In addition, Liu et al. (2021c) proposed to utilize contrastive learning to distill information. Liu et al. (2021a) proposed to use curriculum learning to enhance the performance and Liu et al. (2021b) proposed to explore posterior and prior knowledge for report generation. Yang et al. (2021); Li et al. (2023); Huang et al. (2023) proposed to utilize the external knowledge graph (i.e., RadGraph (Jain et al., 2021)) for report generation.

Other works focused on improving the clinical accuracy and faithfulness of the generated reports. Liu et al. (2019a); Lovelace and Mortazavi (2020); Miura et al. (2021); Nishino et al. (2022); Delbrouck et al. (2022) designed various kinds of rewards (e.g., entity matching score) to improve clinical accuracy via reinforcement learning. Tanida et al. (2023) proposed an explainable framework for report generation that could identify the abnormal areas of a given radiograph. Hou et al. (2023) proposed to combine both textual plans and radiographs to maintain clinical consistency. Additionally, Ramesh et al. (2022) and Bannur et al. (2023) focus on handling the temporal structure in radiology report generation, either removing the prior or learning from the historical records.

6.2 Graph Reasoning for Text Generation

Graph reasoning for text generation (Liu et al., 2019b; Tuan et al., 2022) tries to identify relevant knowledge from graphs and incorporate it into generated text sequences. Huang et al. (2020) proposed to construct a knowledge graph from the input document and utilize it to enhance the performance of abstractive summarization. Ji et al. (2020) proposed to incorporate commonsense knowledge for

language generation via multi-hop reasoning. Mu and Li (2022) proposed to combine both event-level and token-level from the knowledge graph to improve the performance.

7 Conclusion

In this paper, we propose RECAP, which can capture both spatial and temporal information for generating precise and accurate radiology reports. To achieve precise attribute modeling in the generation process, we construct a disease progression graph containing both observations and fined-grained attributes which quantify the severity of diseases and devise a dynamic disease progression reasoning (PrR) mechanism to select observation-relevant attributes. Experimental results demonstrate the effectiveness of our proposed model in terms of generating precise and accurate radiology reports.

Limitations

Our proposed two-stage framework requires predefined observations and progressions for training, which may not be available for other types of radiographs. In addition, the outputs of Stage 1 are the prerequisite inputs of Stage 2, and thus, our framework may suffer from error propagation. Finally, although prior information is important in generating precise and accurate free-text reports, historical records are not always available, even in the two benchmark datasets. Our framework will still generate misleading free-text reports, conditioning on non-existent priors, as indicated in Ramesh et al. (2022). This might be mitigated through rule-based removal operations.

Ethics Statement

The MIMIC-ABN(Ni et al., 2020) and MIMIC-CXR (Johnson et al., 2019) datasets are publicly available benchmarks and have been automatically de-identified to protect patient privacy. Although our model improves the factual accuracy of generated reports, its performance still lags behind the practical deployment. The outputs of our model may contain false observations and diagnoses due to systematic biases. In this regard, we strongly urge the users to examine the generated output in real-world applications cautiously.

Acknolwedgments

This work was supported in part by General Program of National Natural Science Foundation of China (Grant No. 82272086, 62076212), Guangdong Provincial Department of Education (Grant No. 2020ZDZX3043), Shenzhen Natural Science Fund (JCYJ20200109140820699 and the Stable Support Plan Program 20200925174052004), and the Research Grants Council of Hong Kong (15207920, 15207821, 15207122).

References

Peter Anderson, Xiaodong He, Chris Buehler, Damien Teney, Mark Johnson, Stephen Gould, and Lei Zhang. 2018. Bottom-up and top-down attention for image captioning and visual question answering. In *2018 IEEE Conference on Computer Vision and Pattern Recognition, CVPR 2018, Salt Lake City, UT, USA, June 18-22, 2018*, pages 6077–6086. Computer Vision Foundation / IEEE Computer Society.

Satanjeev Banerjee and Alon Lavie. 2005. METEOR: An automatic metric for MT evaluation with improved correlation with human judgments. In *Proceedings of the ACL Workshop on Intrinsic and Extrinsic Evaluation Measures for Machine Translation and/or Summarization*, pages 65–72, Ann Arbor, Michigan. Association for Computational Linguistics.

Shruthi Bannur, Stephanie Hyland, Qianchu Liu, Fernando Pérez-García, Maximilian Ilse, Daniel C. Castro, Benedikt Boecking, Harshita Sharma, Kenza Bouzid, Anja Thieme, Anton Schwaighofer, Maria Wetscherek, Matthew P. Lungren, Aditya Nori, Javier Alvarez-Valle, and Ozan Oktay. 2023. Learning to exploit temporal structure for biomedical vision-language processing.

Zhihong Chen, Yaling Shen, Yan Song, and Xiang Wan. 2021. Cross-modal memory networks for radiology report generation. In *Proceedings of the 59th Annual Meeting of the Association for Computational Linguistics and the 11th International Joint Conference on Natural Language Processing, ACL/IJCNLP 2021, (Volume 1: Long Papers), Virtual Event, August 1-6, 2021*, pages 5904–5914. Association for Computational Linguistics.

Zhihong Chen, Yan Song, Tsung-Hui Chang, and Xiang Wan. 2020. Generating radiology reports via memory-driven transformer. In *Proceedings of the 2020 Conference on Empirical Methods in Natural Language Processing*.

Kenneth Ward Church and Patrick Hanks. 1990. Word association norms, mutual information, and lexicography. *Computational Linguistics*, 16(1):22–29.

Jean-Benoit Delbrouck, Pierre Chambon, Christian Bluethgen, Emily Tsai, Omar Almusa, and Curtis Langlotz. 2022. Improving the factual correctness of radiology report generation with semantic rewards. In *Findings of the Association for Computational*

Linguistics: EMNLP 2022, pages 4348–4360, Abu Dhabi, United Arab Emirates. Association for Computational Linguistics.

Jia Deng, Wei Dong, Richard Socher, Li-Jia Li, Kai Li, and Li Fei-Fei. 2009. Imagenet: A large-scale hierarchical image database. In *2009 IEEE Conference on Computer Vision and Pattern Recognition*, pages 248–255.

Alexey Dosovitskiy, Lucas Beyer, Alexander Kolesnikov, Dirk Weissenborn, Xiaohua Zhai, Thomas Unterthiner, Mostafa Dehghani, Matthias Minderer, Georg Heigold, Sylvain Gelly, Jakob Uszkoreit, and Neil Houlsby. 2021. An image is worth 16x16 words: Transformers for image recognition at scale. In *International Conference on Learning Representations*.

Mark Endo, Rayan Krishnan, Viswesh Krishna, Andrew Y. Ng, and Pranav Rajpurkar. 2021. Retrieval-based chest x-ray report generation using a pre-trained contrastive language-image model. In *Proceedings of Machine Learning for Health*, volume 158 of *Proceedings of Machine Learning Research*, pages 209–219. PMLR.

Wenjun Hou, Kaishuai Xu, Yi Cheng, Wenjie Li, and Jiang Liu. 2023. Organ: Observation-guided radiology report generation via tree reasoning.

Luyang Huang, Lingfei Wu, and Lu Wang. 2020. Knowledge graph-augmented abstractive summarization with semantic-driven cloze reward. In *Proceedings of the 58th Annual Meeting of the Association for Computational Linguistics*, pages 5094–5107, Online. Association for Computational Linguistics.

Zhongzhen Huang, Xiaofan Zhang, and Shaoting Zhang. 2023. Kiut: Knowledge-injected u-transformer for radiology report generation. In *Proceedings of the IEEE/CVF Conference on Computer Vision and Pattern Recognition (CVPR)*, pages 19809–19818.

Jeremy Irvin, Pranav Rajpurkar, Michael Ko, Yifan Yu, Silviana Ciurea-Ilcus, Chris Chute, Henrik Marklund, Behzad Haghgoo, Robyn L. Ball, Katie S. Shpanskaya, Jayne Seekins, David A. Mong, Safwan S. Halabi, Jesse K. Sandberg, Ricky Jones, David B. Larson, Curtis P. Langlotz, Bhavik N. Patel, Matthew P. Lungren, and Andrew Y. Ng. 2019. Chexpert: A large chest radiograph dataset with uncertainty labels and expert comparison. In *The Thirty-Third AAAI Conference on Artificial Intelligence*, pages 590–597.

Saahil Jain, Ashwin Agrawal, Adriel Saporta, Steven Q. H. Truong, Du Nguyen Duong, Tan Bui, Pierre Chambon, Yuhao Zhang, Matthew P. Lungren, Andrew Y. Ng, Curtis P. Langlotz, and Pranav Rajpurkar. 2021. Radgraph: Extracting clinical entities and relations from radiology reports. *CoRR*, abs/2106.14463.

Haozhe Ji, Pei Ke, Shaohan Huang, Furu Wei, Xiaoyan Zhu, and Minlie Huang. 2020. Language generation with multi-hop reasoning on commonsense knowledge graph. In *Proceedings of the 2020 Conference on Empirical Methods in Natural Language Processing (EMNLP)*, pages 725–736, Online. Association for Computational Linguistics.

Baoyu Jing, Pengtao Xie, and Eric P. Xing. 2018. On the automatic generation of medical imaging reports. In *Proceedings of the 56th Annual Meeting of the Association for Computational Linguistics, ACL 2018, Melbourne, Australia, July 15-20, 2018, Volume 1: Long Papers*, pages 2577–2586. Association for Computational Linguistics.

Alistair EW Johnson, Tom J Pollard, Nathaniel R Greenbaum, Matthew P Lungren, Chih-ying Deng, Yifan Peng, Zhiyong Lu, Roger G Mark, Seth J Berkowitz, and Steven Horng. 2019. Mimic-cxr-jpg, a large publicly available database of labeled chest radiographs. *arXiv preprint arXiv:1901.07042*.

Mingjie Li, Bingqian Lin, Zicong Chen, Haokun Lin, Xiaodan Liang, and Xiaojun Chang. 2023. Dynamic graph enhanced contrastive learning for chest x-ray report generation. In *Proceedings of the IEEE/CVF Conference on Computer Vision and Pattern Recognition (CVPR)*, pages 3334–3343.

Yuan Li, Xiaodan Liang, Zhiting Hu, and Eric P. Xing. 2018. Hybrid retrieval-generation reinforced agent for medical image report generation. In *Advances in Neural Information Processing Systems 31: Annual Conference on Neural Information Processing Systems 2018, NeurIPS 2018, December 3-8, 2018, Montréal, Canada*, pages 1537–1547.

Chin-Yew Lin. 2004. ROUGE: A package for automatic evaluation of summaries. In *Text Summarization Branches Out*, pages 74–81, Barcelona, Spain. Association for Computational Linguistics.

Fenglin Liu, Shen Ge, and Xian Wu. 2021a. Competence-based multimodal curriculum learning for medical report generation. In *Proceedings of the 59th Annual Meeting of the Association for Computational Linguistics and the 11th International Joint Conference on Natural Language Processing, ACL/IJCNLP 2021, (Volume 1: Long Papers), Virtual Event, August 1-6, 2021*, pages 3001–3012. Association for Computational Linguistics.

Fenglin Liu, Xian Wu, Shen Ge, Wei Fan, and Yuexian Zou. 2021b. Exploring and distilling posterior and prior knowledge for radiology report generation. In *IEEE Conference on Computer Vision and Pattern Recognition, CVPR 2021, virtual, June 19-25, 2021*, pages 13753–13762. Computer Vision Foundation / IEEE.

Fenglin Liu, Changchang Yin, Xian Wu, Shen Ge, Ping Zhang, and Xu Sun. 2021c. Contrastive attention for automatic chest x-ray report generation. In *Findings of the Association for Computational Linguistics: ACL/IJCNLP 2021, Online Event, August 1-6, 2021*, volume ACL/IJCNLP 2021 of *Findings of ACL*, pages 269–280. Association for Computational Linguistics.

Guanxiong Liu, Tzu-Ming Harry Hsu, Matthew B. A. McDermott, Willie Boag, Wei-Hung Weng, Peter Szolovits, and Marzyeh Ghassemi. 2019a. Clinically accurate chest x-ray report generation. *CoRR*, abs/1904.02633.

Zhibin Liu, Zheng-Yu Niu, Hua Wu, and Haifeng Wang. 2019b. Knowledge aware conversation generation with explainable reasoning over augmented graphs. In *Proceedings of the 2019 Conference on Empirical Methods in Natural Language Processing and the 9th International Joint Conference on Natural Language Processing (EMNLP-IJCNLP)*, pages 1782–1792, Hong Kong, China. Association for Computational Linguistics.

Ilya Loshchilov and Frank Hutter. 2019. Decoupled weight decay regularization. In *7th International Conference on Learning Representations, ICLR 2019, New Orleans, LA, USA, May 6-9, 2019*. OpenReview.net.

Justin Lovelace and Bobak Mortazavi. 2020. Learning to generate clinically coherent chest X-ray reports. In *Findings of the Association for Computational Linguistics: EMNLP 2020*, pages 1235–1243, Online. Association for Computational Linguistics.

Jiasen Lu, Caiming Xiong, Devi Parikh, and Richard Socher. 2017. Knowing when to look: Adaptive attention via a visual sentinel for image captioning. In *2017 IEEE Conference on Computer Vision and Pattern Recognition, CVPR 2017, Honolulu, HI, USA, July 21-26, 2017*, pages 3242–3250. IEEE Computer Society.

Yasuhide Miura, Yuhao Zhang, Emily Tsai, Curtis Langlotz, and Dan Jurafsky. 2021. Improving factual completeness and consistency of image-to-text radiology report generation. In *Proceedings of the 2021 Conference of the North American Chapter of the Association for Computational Linguistics: Human Language Technologies*, pages 5288–5304, Online. Association for Computational Linguistics.

Feiteng Mu and Wenjie Li. 2022. Enhancing text generation via multi-level knowledge aware reasoning. In *Proceedings of the Thirty-First International Joint Conference on Artificial Intelligence, IJCAI-22*, pages 4310–4316. International Joint Conferences on Artificial Intelligence Organization. Main Track.

Jianmo Ni, Chun-Nan Hsu, Amilcare Gentili, and Julian McAuley. 2020. Learning visual-semantic embeddings for reporting abnormal findings on chest X-rays. In *Findings of the Association for Computational Linguistics: EMNLP 2020*, pages 1954–1960, Online. Association for Computational Linguistics.

Toru Nishino, Yasuhide Miura, Tomoki Taniguchi, Tomoko Ohkuma, Yuki Suzuki, Shoji Kido, and Noriyuki Tomiyama. 2022. Factual accuracy is not enough: Planning consistent description order for radiology report generation. In *Proceedings of the 2022 Conference on Empirical Methods in Natural Language Processing*, Online. Association for Computational Linguistics.

Farhad Nooralahzadeh, Nicolas Perez Gonzalez, Thomas Frauenfelder, Koji Fujimoto, and Michael Krauthammer. 2021. Progressive transformer-based generation of radiology reports. In *Findings of the Association for Computational Linguistics: EMNLP 2021*, pages 2824–2832, Punta Cana, Dominican Republic. Association for Computational Linguistics.

Kishore Papineni, Salim Roukos, Todd Ward, and Wei-Jing Zhu. 2002. Bleu: a method for automatic evaluation of machine translation. In *Proceedings of the 40th Annual Meeting of the Association for Computational Linguistics*, pages 311–318, Philadelphia, Pennsylvania, USA. Association for Computational Linguistics.

Han Qin and Yan Song. 2022. Reinforced cross-modal alignment for radiology report generation. In *Findings of the Association for Computational Linguistics: ACL 2022, Dublin, Ireland, May 22-27, 2022*, pages 448–458. Association for Computational Linguistics.

Vignav Ramesh, Nathan Andrew Chi, and Pranav Rajpurkar. 2022. Improving radiology report generation systems by removing hallucinated references to nonexistent priors.

Steven J. Rennie, Etienne Marcheret, Youssef Mroueh, Jerret Ross, and Vaibhava Goel. 2017. Self-critical sequence training for image captioning. In *2017 IEEE Conference on Computer Vision and Pattern Recognition, CVPR 2017, Honolulu, HI, USA, July 21-26, 2017*, pages 1179–1195. IEEE Computer Society.

Michael Schlichtkrull, Thomas N Kipf, Peter Bloem, Rianne van den Berg, Ivan Titov, and Max Welling. 2018. Modeling relational data with graph convolutional networks. In *European semantic web conference*, pages 593–607. Springer.

Akshay Smit, Saahil Jain, Pranav Rajpurkar, Anuj Pareek, Andrew Ng, and Matthew Lungren. 2020. Combining automatic labelers and expert annotations for accurate radiology report labeling using BERT. In *Proceedings of the 2020 Conference on Empirical Methods in Natural Language Processing (EMNLP)*, pages 1500–1519, Online. Association for Computational Linguistics.

Xiao Song, Xiaodan Zhang, Junzhong Ji, Ying Liu, and Pengxu Wei. 2022. Cross-modal contrastive attention model for medical report generation. In *Proceedings of the 29th International Conference on Computational Linguistics*, pages 2388–2397, Gyeongju, Republic of Korea. International Committee on Computational Linguistics.

Tim Tanida, Philip Müller, Georgios Kaissis, and Daniel Rueckert. 2023. Interactive and explainable region-guided radiology report generation. In *Proceedings of the IEEE/CVF Conference on Computer Vision and Pattern Recognition (CVPR)*, pages 7433–7442.

Yi-Lin Tuan, Sajjad Beygi, Maryam Fazel-Zarandi, Qiaozi Gao, Alessandra Cervone, and William Yang Wang. 2022. Towards large-scale interpretable knowledge graph reasoning for dialogue systems. In *Findings of the Association for Computational Linguistics: ACL 2022*, pages 383–395, Dublin, Ireland. Association for Computational Linguistics.

Ashish Vaswani, Noam Shazeer, Niki Parmar, Jakob Uszkoreit, Llion Jones, Aidan N. Gomez, Łukasz Kaiser, and Illia Polosukhin. 2017. Attention is all you need. In *Proceedings of the 31st International Conference on Neural Information Processing Systems*, NIPS'17, page 6000–6010, Red Hook, NY, USA. Curran Associates Inc.

Oriol Vinyals, Alexander Toshev, Samy Bengio, and Dumitru Erhan. 2015. Show and tell: A neural image caption generator. In *CVPR*, pages 3156–3164. IEEE Computer Society.

Zhanyu Wang, Lingqiao Liu, Lei Wang, and Luping Zhou. 2023. Metransformer: Radiology report generation by transformer with multiple learnable expert tokens. In *Proceedings of the IEEE/CVF Conference on Computer Vision and Pattern Recognition (CVPR)*, pages 11558–11567.

Thomas Wolf, Lysandre Debut, Victor Sanh, Julien Chaumond, Clement Delangue, Anthony Moi, Pierric Cistac, Tim Rault, Remi Louf, Morgan Funtowicz, Joe Davison, Sam Shleifer, Patrick von Platen, Clara Ma, Yacine Jernite, Julien Plu, Canwen Xu, Teven Le Scao, Sylvain Gugger, Mariama Drame, Quentin Lhoest, and Alexander Rush. 2020. Transformers: State-of-the-art natural language processing. In *Proceedings of the 2020 Conference on Empirical Methods in Natural Language Processing: System Demonstrations*, pages 38–45, Online. Association for Computational Linguistics.

Joy T Wu, Nkechinyere Nneka Agu, Ismini Lourentzou, Arjun Sharma, Joseph Alexander Paguio, Jasper Seth Yao, Edward Christopher Dee, William G Mitchell, Satyananda Kashyap, Andrea Giovannini, Leo Anthony Celi, and Mehdi Moradi. 2021. Chest imagenome dataset for clinical reasoning. In *Thirty-fifth Conference on Neural Information Processing Systems Datasets and Benchmarks Track (Round 2)*.

Shuxin Yang, Xian Wu, Shen Ge, Shaohua Kevin Zhou, and Li Xiao. 2021. Knowledge matters: Radiology report generation with general and specific knowledge. *CoRR*, abs/2112.15009.

A Appendix

A.1 Observation and Progression Statitics

There are 14 observations: No Finding, Enlarged Cardiomediastinum, Cardiomegaly, Lung Lesion, Lung Opacity, Edema, Consolidation, Pneumonia, Atelectasis, Pneumothorax, Pleural Effusion, Pleural Other, Fracture, and Support Devices. Table 5 lists the observation distributions annotated by CheXbert(Smit et al., 2020) in the train/valid/test split of two benchmarks and Table 7 shows the progression distributions in our experiments.

#Observation	MIMIC-ABN	MIMIC-CXR
No Finding/POS	5002/32/22	64,677/514/229
No Finding/NEG	66,784/514/784	206,133/1,616/3,629
Cardiomegaly/POS	16,312/118/244	70,561/514/1,602
Cardiomegaly/NEG	804/4/8	85,448/714/801
Pleural Effusion/POS	10,502/80/186	56,972/477/1,379
Pleural Effusion/NEG	1,948/18/24	170,989/1,310/1,763
Pneumothorax/POS	1,452/24/4	8,707/62/106
Pneumothorax/NEG	1,792/10/26	190,356/1,495/2,338
Enlarged Card./POS	5,202/40/90	49,806/413/1,140
Enlarged Card./NEG	1,194/10/14	129,360/1,006/868
Consolidation/POS	4,104/36/96	14,449/119/384
Consolidation/NEG	3,334/20/34	97,197/788/964
Lung Opacity/POS	22,598/166/356	67,714/497/1,448
Lung Opacity/NEG	748/10/4	8,157/73/125
Fracture/POS	4,458/32/76	11,070/59/232
Fracture/NEG	330/0/0	9,632/72/53
Lung Lesion/POS	5,612/54/112	11,717/123/300
Lung Lesion/NEG	120/2/2	1,972/21/11
Edema/POS	8,704/76/168	33,034/257/899
Edema/NEG	1,898/16/32	51,639/409/669
Atelectasis/POS	19,132/134/220	68,273/515/1,210
Atelectasis/NEG	116/2/0	563/5/9
Support Devices/POS	9,886/58/196	60,455/450/1,358
Support Devices/NEG	394/0/10	1,081/7/11
Pneumonia/POS	17,826/138/260	23,945/184/503
Pneumonia/NEG	3,226/22/34	21,976/165/411
Pleural Other/POS	2,850/30/62	7,296/70/184
Pleural Other/NEG	8/0/0	63/0/0

Table 5: Observation distribution in train/valid/test split of two benchmarks. *Enlarged Card.* refers to *Enlarged Cardiomediastinum*.

A.2 Spatial and Temporal Entity

Here are some of the spatial entities: healed, fractured, healing, nondisplaced, top, size, heart, normal, mediastinum, widening, contour, widened, consolidative, collapse, underlying, developing, fibrosis, thickening, biapical, blunting, indistinctness, asymmetrical, haziness, asymmetric, layering, subpulmonic, thoracentesis, trace, small, adjacent, tiny, atypical, developing, supervening, multifocal, correct, superimposed, patchy, and borderline. For temporal entities, we use the same settings of Bannur et al. (2023), which are: bigger, change, cleared, constant, decrease, decreased, decreasing, elevated, elevation, enlarged, enlargement, enlarging, expanded, greater, growing, improved, improvement, improving, increase, increased, increasing, larger, new, persistence, persistent, persisting, progression, progressive, reduced, removal, resolution, resolved, resolving, smaller, stability, stable, stably, unchanged, unfolded, worse, worsen, wors-

Dataset	Model	NLG Metrics						CE Metrics		
		B-1	B-2	B-3	B-4	MTR	R-L	P	R	F_1
w. Historical Record D^p										
MIMIC-ABN	RECAP	0.327	0.183	0.117	0.081	0.124	0.227	0.274	0.372	0.297
	RECAP *w/o* OP	0.300	0.164	0.106	0.072	0.110	0.217	0.281	0.274	0.257
	RECAP *w/o* Obs	0.306	0.173	0.110	0.076	0.114	0.233	0.270	0.288	0.259
	RECAP *w/o* Pro	0.295	0.158	0.099	0.070	0.109	0.209	0.249	0.361	0.278
	RECAP *w/o* PrR	0.320	0.177	0.112	0.076	0.121	0.218	0.266	0.377	0.292
MIMIC-CXR	RECAP	0.423	0.260	0.170	0.118	0.169	0.279	0.387	0.457	0.400
	RECAP *w/o* OP	0.321	0.196	0.131	0.093	0.130	0.260	0.350	0.238	0.256
	RECAP *w/o* Obs	0.347	0.213	0.144	0.104	0.141	0.270	0.465	0.293	0.307
	RECAP *w/o* Pro	0.396	0.236	0.151	0.103	0.153	0.266	0.383	0.447	0.395
	RECAP *w/o* PrR	0.420	0.257	0.168	0.115	0.166	0.279	0.386	0.459	0.403
w/o Historical Record D^p										
MIMIC-ABN	RECAP	0.319	0.182	0.116	0.080	0.120	0.223	0.306	0.360	0.306
	RECAP *w/o* OP	0.303	0.171	0.109	0.074	0.110	0.217	0.299	0.302	0.283
	RECAP *w/o* Obs	0.301	0.174	0.114	0.079	0.114	0.231	0.353	0.313	0.282
	RECAP *w/o* Pro	0.309	0.171	0.109	0.073	0.115	0.222	0.314	0.360	0.302
	RECAP *w/o* PrR	0.320	0.181	0.116	0.079	0.120	0.225	0.299	0.362	0.302
MIMIC-CXR	RECAP	0.427	0.268	0.180	0.128	0.168	0.294	0.378	0.417	0.374
	RECAP *w/o* OP	0.371	0.236	0.164	0.121	0.130	0.260	0.357	0.259	0.268
	RECAP *w/o* Obs	0.363	0.231	0.161	0.119	0.146	0.291	0.415	0.262	0.277
	RECAP *w/o* Pro	0.406	0.251	0.151	0.103	0.153	0.266	0.364	0.405	0.365
	RECAP *w/o* PrR	0.412	0.257	0.172	0.122	0.163	0.289	0.364	0.414	0.368

Table 6: Ablation results of our model and its variants on progression modeling. RECAP *w/o* OP is the standard Transformer model, *w/o* Obs stands for without observation, and *w/o* Pro stands for without progression.

#Progression	MIMIC-ABN	MIMIC-CXR
`Better`	929/2/19	14,790/110/345
`Worse`	1,219/6/30	18,083/163/431
`Stable`	4,114/31/99	41,721/334/1,085
Total	6,440/48/137	64,498/535/1,566
Ratio	9%/8.8%/17%	24%/25.1%/40.6%

Table 7: Progression distribution in train/valid/test split of two benchmarks.

ened, worsening and unaltered.

A.3 Other Implementation Details

Data Preprocessing. We adopt the preprocessing setup used in Chen et al. (2020), and the minimum count of each token is set to 3/10 for MIMIC-ABN/MIMIC-CXR, respectively. Other tokens are replaced with a special token `[UNK]`.

Implementation Details of Stage 1 Training. Table 8 shows the hyperparameters used in Stage 1 training for two datasets. Note that l_{d_i} is the weight for observation detection, and the weights of observation classification and progression classification are both set to 1. In addition, two data augmentation methods are used during training. Specifically, we first resize an input image to 256×256, and then the image is randomly cropped to 224×224, and finally, we flip the image horizontally with a probability of 0.5. We select the best checkpoint based on the Macro-F_1 of abnormal observations at this stage.

Hyperparameter	MIMIC-ABN	MIMIC-CXR
Training Epoch	10	5
Dropout Rate	0.1	0.1
Learning Rate	$1e-4$	$1e-4$
Batch Size	$\{64, \mathbf{128}\}$	$\{64, \mathbf{128}\}$
Sample Weight (α_d)	$\{1, 2, \mathbf{3}\}$	$\{1, 2, \mathbf{3}\}$

Table 8: Selected hyperparameters of Stage 1 training. The final hyperparameters in **boldface** are tuned on the validation set and others are set empirically.

Implementation Details of Stage 2 Training. As the variant *w/o* OP and the variant *w/o* Obs in Table 4 are not trained in Stage 1, they are trained with more epochs (i.e., 10 epochs).

A.4 Other Experimental Results

We show experimental results of observation prediction and progression prediction during Stage 1

training in Table 9 and Table 10, respectively.

Dataset	D-F_1	A-F_1	N-F_1
MIMIC-ABN	0.539	0.355	0.426
MIMIC-CXR	0.686	0.428	0.759

Table 9: Experimental results of observation prediction after Stage 1 training. D-F_1, A-F_1, and N-F_1 denote the F_1 of observation detection, abnormal observation prediction, and normal observation prediction, respectively.

Dataset	Better	Worse	Stable	Macro
MIMIC-ABN	0.286	0.468	0.934	0.563
MIMIC-CXR	0.389	0.455	0.896	0.580

Table 10: Experimental results of progression prediction (F_1) after Stage 1 training.

Observation	P	R	F_1
Enlarged Card.	0.323	0.589	0.417
Cardiomegaly	0.585	0.836	0.689
Lung Opacity	0.489	0.499	0.494
Lung Lesion	0.265	0.044	0.075
Edema	0.562	0.587	0.574
Consolidation	0.285	0.233	0.256
Pneumonia	0.242	0.444	0.313
Atelectasis	0.426	0.800	0.556
Pneumothorax	0.265	0.167	0.205
Pleural Effusion	0.691	0.781	0.728
Pleural Other	0.184	0.050	0.078
Fracture	0.155	0.081	0.107
Support Devices	0.720	0.660	0.689
No Finding	0.265	0.429	0.327
Macro Average	0.389	0.443	0.393

Table 11: Experimental results of each observation after Stage 2 training.